Dislocation mediated continuum plasticity: case studies on modeling scale dependence, scale-invariance, and directionality of sharp yield-point

C. Fressengeas, A. Acharya and A.J. Beaudoin

1 Introduction

Plasticity of crystalline solids is a dynamic phenomenon resulting from the motion under stress of linear crystal defects known as dislocations. Such a statement is grounded on numerous convincing observations, and it is widely accepted by the scientific community. Nevertheless, the conventional plasticity theories use macroscopic variables whose definition does not involve the notion of dislocation. This paradoxical situation arises from the enormous range covered by the length scales involved in the description of plasticity, from materials science to engineering. It may have seemed impossible to account for the astounding complexity of the (microscopic) dynamics of dislocation ensembles at the (macroscopic) scale of the mechanical properties of materials. Justifications offered for such a simplification usually reside in perfect disorder assumptions. Namely, plastic strain is regarded as resulting from a large number of randomly distributed elementary dislocation glide events, showing no order whatsoever at any intermediate length scale. Hence, deriving the mechanical properties from the interactions of dislocations with defects simply requires averaging on any space and time domain. The existence of grain boundaries in polycrystals is of course affecting this averaging

C. Fressengeas
Laboratoire de Physique et Mécanique des Matériaux,
Université Paul Verlaine - Metz / CNRS, Ile du Saulcy, 57045 Metz Cedex, France

A. Acharya
Department of Civil and Environmental Engineering
Carnegie Mellon University, Pittsburgh, PA 15213, USA

A.J. Beaudoin
Department of Mechanical Sciences and Engineering
University of Illinois at Urbana Champaign, Urbana, IL 61801, USA

procedure, but it does not change it fundamentally.

This straightforward jump from microscopic to macroscopic scale has long been the prevailing point of view in the mechanical science as well as in the materials science community. It may be justified for example in bcc materials at low temperature, where the motion of dislocations is subject to large lattice friction. However it reaches its limits when elastic interactions between dislocations become of the order of the interactions with other obstacles to their motion (lattice friction, solute atoms, precipitates....). Since dislocation densities commonly increase during material loading, such a situation is met sooner or later when strain increases. The field of elastic interactions between dislocations then becomes able to generate collective behavior and self-organized phenomena at some intermediate length scale. Collective phenomena include dislocation patterning and the emergence of complex dynamic regimes [1]. Numerous examples of dislocation patterns, involving dislocation - rich and dislocation - poor areas, are observed in optical or electronic microscopy. Such is the case of the dislocation walls formed in cyclic loading (see Figure 1), of dislocation cells (Figure 2) and localized slip bands on the surface of single crystals (Figure 3). Similar spatial structures can also be inferred from

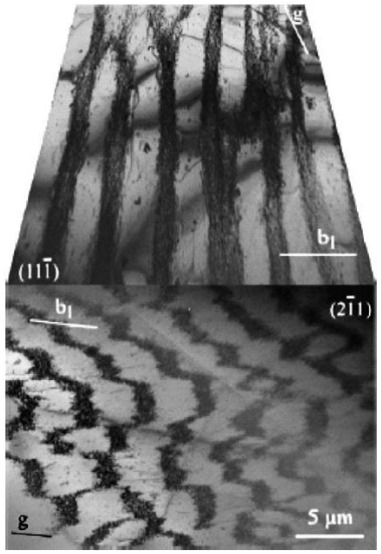

Fig. 1 Dislocation walls in Si single crystal cyclically loaded in tension - compression at high temperature; after [2].

the complex temporal behavior inherent to deformation curves in certain metallic alloys (Portevin - Le Chatelier effect, Lüders bands...) [1]. In such

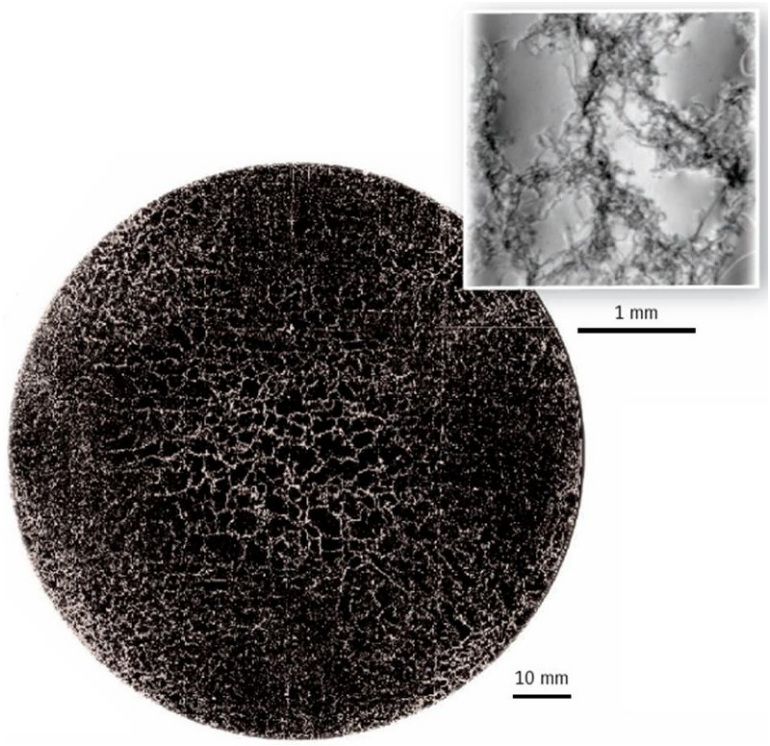

Fig. 2 Optical micrography of giant dislocation cells after $GaAs$ crystal growth. Note that the average cell size varies in inverse proportion to stress. Inset : dislocation cells through X-ray imaging : dark areas are images of lattice distortion around dislocations; after [3].

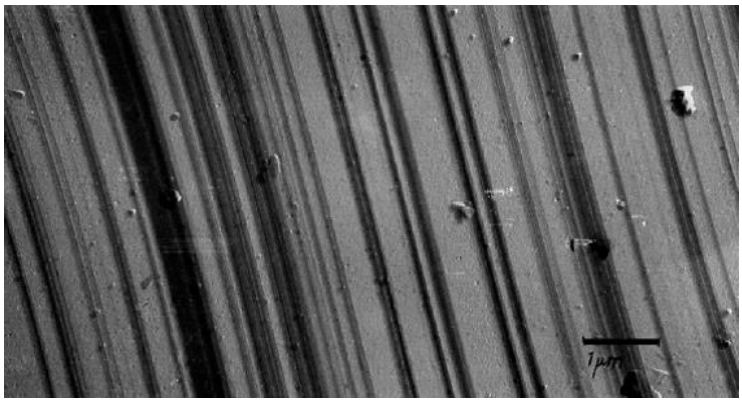

Fig. 3 Slip lines on the surface of $Cu30at\%Zn$ single crystal strained in tension at 19.4% and 77K ; after [4].

conditions, the simple averaging procedures alluded to above are no longer justified. Thus, the conventional theories of plasticity are no longer valid and they are unable to account for the emerging patterns, because they lack the relevant internal length scales.

In attempting to account for self-organization phenomena, a first approach consisted in using strain gradients and rotation gradients in the description of the kinematics of the transformation and introducing the necessary length scales in a phenomenological way into the constitutive equations of plasticity [5, 6, 7, 8]. Such approaches can be referred to as "nonlocal" theories, as opposed to the "local" conventional plasticity theories and they are known as "strain gradient" plasticity theories. They may be useful in the characterization of the emerging patterns, but the identification of the involved length scales, as well as their physical justification may raise difficulties. Further, additional boundary conditions of higher order may be required. The notion that necessary ingredients for the dynamic description of the emerging patterns are the areal dislocation densities defined in a continuous manner over surfaces of appropriate dimensions is recent [9], although these dislocation densities were known for a much longer time [10, 11, 12, 13, 14]. In a way to be documented hereafter, a change of scale must be performed to proceed from individual dislocations to dislocation densities [15]. Clearly, the scale of resolution must be smaller than the characteristic length scale of the dislocation patterns to be described. However, there is no mandatory rule, and the choice of the resolution length scale depends on the accuracy demanded on the description. Hence, a phenomenon deemed "non - local" in a fine scale resolution scheme may well be classified as "local" when the scale of resolution is sufficiently enlarged. Further, when envisioned on such intermediate resolution length scales, dislocation motion is amenable to transport of the areal dislocation densities, which confers propagative character to these variables, in connection with the equation for dislocation transport [11, 12]. Fundamental changes in the mathematical nature of the governing equations derive from this property and impact on the algorithms devoted to the solution of boundary value problems [16, 17, 18].

The stress field responsible for the nucleation and motion of dislocations derives in the first place from the tractions and displacements imposed on the sample boundaries. When the distribution of dislocations becomes inhomogeneous at some chosen scale, their long - range internal stress field brings about a redistribution of stresses and dislocations, in a manner accounting for the elastic properties of the material, stress equilibrium and boundary conditions. Along this process, the evolution of the dislocation density and internal stress fields depends on the strain path and anisotropy is induced. The objective assigned to field dislocation dynamics theories is to account for the emergence of inhomogeneous dislocation distributions at some mesoscopic (intermediate) length scale, as well as their consequences on mechan-

ical behavior. Three such problems will be reviewed in the present Chapter. First, field dislocation dynamics theories are obviously well suited for small size systems: nano-structures, micro-systems... Here, the overall dimensions of the sample are not much larger than the characteristic length scale of the dislocation patterns and, consequently, effects of sample size on mechanical response are to be observed. Interpretation of these size effects through field dislocation dynamics [19] will be discussed in the following. Secondly, since dislocations are often conveniently viewed as distinct objects, dislocation activity appears to be inhomogeneous at a finer scale of resolution. Because dislocation glide is controlled by local obstacles in a large class of materials, it is also intermittent in time. In these materials, dislocation motion consists in successive fast runs of dislocation segments from one obstacle to the next one, with the flight time of dislocations being much smaller than their arrest time on obstacles. Although intermittency of plasticity was described as early as 1932 in Zn single crystals [20], the prevailing interpretation has been perfect disorder. In average over sufficiently large length and time scales, intermittent fluctuations have been regarded as adding at random to a smooth in time and homogeneous in space net response. A fundamentally different understanding emerged during the last few years when statistical analysis of these fluctuations became available, that of a scale-invariant phenomenon characterized by power law distributions of fluctuation size, and correlations in space and time [21, 22, 23, 24, 25]. Because they feature correlations in space due to both the long-range internal stresses and the short-range interactions involved in dislocation transport, field dislocation dynamics theories are candidates for the interpretation of scale-invariant intermittency [26], and the results will be reported herein. Finally, the anisotropy of strain hardening induced by the emergence of internal stress fields will be reviewed. The directionality of the sharp yield point in strain-aged steels and the occurrence of a Baushinger effect after a sequence of forward-reverse straining will receive interpretation within the framework of a field dislocation theory coupling the evolution of statistical and polar dislocation densities with that of point defects due to strain-aging [27].

By considering internal stresses due to dislocation - dislocation interactions, alternative modeling approaches such as statistical mechanics [4], phase field [28] and discrete dislocation dynamics methods [22, 29, 30] reproduce the scale-invariance of plastic activity. They have a potential for retrieving length-scale dependence of material properties, but usually consider periodic boundary conditions over small domains. Further, both phase field and statistical mechanics methods have not been shown to retrieve the propagative features related with dislocation transport. In discrete dislocation dynamics simulations, transport of dislocation densities is present, but fully resolved into the motion of individual dislocations. As a rule of thumb, using present day computing facilities, dislocation dynamics codes are able to handle a tenfold increase of the initial number of dislocations [31]. Hence, dislocations dy-

namics simulations are still limited to small size / small strain systems, with a simulation box size of the order of $10\mu m^3$ and a plastic strain achieved amounting to about 10^{-2}. Thus, if not for the treatment of boundary conditions, geometric and elastic nonlinearity, and inertia, the chances to tackle large-scale engineering problems in the future with discrete dislocation dynamics simulations are slim, and field dislocation theories seem to be more fitted for real scale boundary value problems.

The Chapter is organized as follows. In Section 2, we provide an overview of the current field dislocation dynamics theories, augmented with recent developments in macroscopic polycrystal response. Section 3 deals with the effects of sample size on mechanical response, and is illustrated with the example of ice single crystals submitted to torsion creep where robust size effects are observed. Section 4 is devoted to scale-invariance and transport effects in the intermittency of crystal plasticity. Examples include the behavior of copper single crystals in tension. Section 5 deals with the anisotropy in mechanical properties induced by complex strain paths, with the exemple of the directionality of the sharp yield point and the occurrence of a Baushinger effect in strain-aged polycrystalline steels. The concluding section provides insights into the flexibility of the theory regarding the scale of resolution and its ability to deal with fine - scale vs. engineering - scale simulations.

2 Field dislocation dynamics theory

The theory uses the continuum description of dislocations based upon Nye's dislocation density tensor $\boldsymbol{\alpha}$ [10]. Operating on the normal $\mathbf{n}$ to a unit surface S, $\boldsymbol{\alpha}$ provides the net Burgers vector $\mathbf{b} = \boldsymbol{\alpha}.\mathbf{n}$ of all dislocations lines threading S, *i.e.*, the incompatibility in plastic displacement found along the Burgers circuit C surrounding S. When surface S is so small that it is threaded by a single dislocation with Burgers vector $\mathbf{b}$ and line vector $\mathbf{t}$, $\boldsymbol{\alpha} = \mathbf{b} \otimes \mathbf{t}$ and the involved dislocation is labelled as a "polar dislocation". When the size of S, *i.e.*, the resolution length scale, is increased to the point where S is threaded by a large number of dislocations, $\mathbf{b}$ may be zero if all individual Burgers vectors statistically offset. Then $\boldsymbol{\alpha}$ is zero, the dislocations are unresolved and they are deemed "statistical". In intermediate cases, the net Burgers vector $\mathbf{b}$ is non-zero, but part of the dislocations threading S may remain unresolved. The subscripts in the density components α_{ij} then indicate respectively the net Burgers vector and line vector directions of polar dislocations, whereas the remaining statistical dislocations are not accounted for in tensor $\boldsymbol{\alpha}$. Due to lattice incompatibility, the plastic distortion tensor $\mathbf{U_p}$ is not a gradient; it is written as a sum of a gradient and an incompatible part that cannot be expressed as a gradient

$$\mathbf{U_p} = \mathbf{grad}\ \mathbf{z} - \boldsymbol{\chi} \tag{1}$$

The incompatible part results from the distribution $\boldsymbol{\alpha}$ through the fundamental geometrical equation of incompatibility

$$\mathbf{curl}\ \mathbf{U_p} = -\mathbf{curl}\ \boldsymbol{\chi} = -\boldsymbol{\alpha} \tag{2}$$

augmented with the side conditions

$$\mathbf{div}\ \boldsymbol{\chi} = 0 \tag{3}$$

and $\boldsymbol{\chi}.\mathbf{n} = 0$ on the boundary with unit normal $\mathbf{n}$, to ensure that when $\boldsymbol{\alpha} = 0$ the incompatible part $\boldsymbol{\chi}$ vanishes identically on the body. The compatible part depends upon the history of plastic straining and records the compatible increments of the plastic strain rate produced by the motion of dislocations through the equation

$$\mathbf{div}\ \mathbf{grad}\ \dot{\mathbf{z}} = \mathbf{div}\ (\boldsymbol{\alpha} \times \mathbf{V}) \tag{4}$$

where the field $\mathbf{V}$ represents the velocity of an infinitesimal dislocation segment at any spatio-temporal location. In this model of dislocation mechanics, the total displacement field, $\mathbf{u}$, does not represent the actual physical motion of atoms involving topological changes but only a consistent shape change and hence is not required to be discontinuous. However, the stress produced by these topological changes in the lattice is adequately reflected in the theory through the utilization of incompatible elastic/plastic distortions. As usual in continuum plasticity, the elastic distortion (nonsymmetric) is assumed to be the difference of the total displacement gradient and the plastic distortion

$$\mathbf{U_e} := \mathbf{grad}\ \mathbf{u} - \mathbf{U_p} \tag{5}$$

and the stress is a function of the elastic distortion (in the linear elastic case given by $\mathbf{T} = \mathbf{C} : \mathbf{U_e}$) satisfying the equation of equilibrium

$$\mathbf{div}\ \mathbf{T} = \mathbf{0} \tag{6}$$

Finally, $\boldsymbol{\alpha}$ evolves according to the fundamental transport law, which derives from the conservation of Burgers vector content

$$\dot{\boldsymbol{\alpha}} = -\mathbf{curl}\ (\boldsymbol{\alpha} \times \mathbf{V}) \tag{7}$$

Gathering all equations, the complete theory reads as

$$\mathbf{curl}\ \boldsymbol{\chi} = \boldsymbol{\alpha} \tag{8}$$

$$\mathbf{div}\ \boldsymbol{\chi} = 0 \tag{9}$$

$$\mathbf{div}\ \mathbf{grad}\ \dot{\mathbf{z}} = \mathbf{div}\ (\boldsymbol{\alpha} \times \mathbf{V}) \tag{10}$$

$$\mathbf{div}\ [\mathbf{C} : \{\mathbf{grad}\ (\mathbf{u} - \mathbf{z}) + \boldsymbol{\chi}\}] = 0 \tag{11}$$

$$\dot{\boldsymbol{\alpha}} = -\mathbf{curl}\,(\boldsymbol{\alpha} \times \mathbf{V}) \tag{12}$$

To derive the structure of an averaged mesoscopic theory, we adapt an averaging procedure commonly used in the study of multiphase flows (see, e.g., [32]). For a microscopic field f given as a function of space and time, we define the mesoscopic space-time averaged field $\bar{f}$ as

$$\bar{f}(\mathbf{x},t) = \frac{1}{\int_{I(t)}\int_{\Omega(x)} w(\mathbf{x}-\mathbf{x}',t-t')d\mathbf{x}'dt'} \int_{\Im}\int_{B} w(\mathbf{x}-\mathbf{x}',t-t')f(\mathbf{x}',t')\,d\mathbf{x}'\,dt' \tag{13}$$

where B is the body and $\Im$ a sufficiently large interval of time. In the above, $\Omega(\mathbf{x})$ is a bounded region within the body around point $\mathbf{x}$ with linear dimension of the order of the spatial resolution of the macroscopic model we seek, and $I(t)$ is a bounded interval in $\Im$ containing t. The weighting function w is non-dimensional, assumed to be smooth in the variables $(\mathbf{x},\mathbf{x}',t,t')$ and, for fixed $\mathbf{x}$ and t, has support (*i.e.* is non-zero) only in the domain $\Re = \Omega(\mathbf{x}) \times I(t)$ when viewed as a function of $(\mathbf{x}',t')$. The averaged field $\bar{f}$ is simply a weighted, space-time running average of the microscopic field f over $\Re$, whose scale is determined by the scale of spatial and temporal resolution of the averaged model one seeks. Applying this operator to Eqs. (8-12), we obtain [15] an exact set of equations for the averages given as

$$\mathbf{curl}\;\bar{\chi} = \bar{\alpha} \tag{14}$$

$$\mathbf{div}\;\bar{\chi} = 0 \tag{15}$$

$$\mathbf{div\;grad}\;\dot{\bar{z}} = \mathbf{div}\;(\bar{\alpha} \times \bar{\mathbf{V}} + \mathbf{L_p}) \tag{16}$$

$$\mathbf{div}\;[\mathbf{C} : \{\mathbf{grad}\;(\bar{\mathbf{u}} - \bar{\mathbf{z}}) + \bar{\chi}\}] = 0 \tag{17}$$

$$\dot{\bar{\alpha}} = -\mathbf{curl}\;(\bar{\alpha} \times \bar{\mathbf{V}} + \mathbf{L_p}) \tag{18}$$

where $\mathbf{L_p}$, defined as

$$\mathbf{L_p} := \overline{(\boldsymbol{\alpha} - \bar{\boldsymbol{\alpha}}) \times \mathbf{V}}(\mathbf{x},t) = \overline{\boldsymbol{\alpha} \times \mathbf{V}}(\mathbf{x},t) - \bar{\boldsymbol{\alpha}} \times \bar{\mathbf{V}}(\mathbf{x},t), \tag{19}$$

and $\bar{\mathbf{V}}$ are the terms that require closure. Physically, $\mathbf{L_p}$ is representative of a portion of the average slip strain rate produced by the "microscopic" dislocation density; in particular, it can be non-vanishing even when $\bar{\boldsymbol{\alpha}} = 0$ and, as such, it is to be physically interpreted as the strain-rate produced by the so-called "statistical dislocations", as is also indicated by the extreme right-hand side of (19). The variable $\bar{\mathbf{V}}$ has the obvious physical meaning of being a space-time average of the point-wise, microscopic dislocation velocity. Initial and boundary conditions for (8-12) are important from the physical modeling point of view [15], particularly in the context of triggering inhomogeneity under boundary conditions corresponding to homogeneous deformation in conventional plasticity theory [17].

It is possible to eliminate the fields $(\boldsymbol{\chi},\mathbf{z})$ (dropping overhead bars for convenience) in the set of equations (14-18), *provided that the continuity*

conditions implied by the set of equations at surfaces of discontinuity are retained. Considering for simplicity discontinuity surfaces that do not move with respect to the material, a reduced set of equations can be written as

$$\mathbf{div}\ \mathbf{T} = 0 \tag{20}$$

$$\mathbf{T} = \mathbf{C} : \mathbf{U_e} \tag{21}$$

$$\mathbf{U_e} = \mathbf{grad}\ \mathbf{u} - \mathbf{U_p} \tag{22}$$

$$\dot{\mathbf{U}}_\mathbf{p} = \boldsymbol{\alpha} \times \mathbf{V} + \mathbf{L_p} \tag{23}$$

$$\dot{\boldsymbol{\alpha}} = -\mathbf{curl}\ \dot{\mathbf{U}}_\mathbf{p} \tag{24}$$

$$\left[\dot{\mathbf{U}}_\mathbf{p}\right] \times \mathbf{n} = 0 \tag{25}$$

where $\left[\mathbf{A}\right]$ represents a jump of $\mathbf{A}$ at the surface of discontinuity and $\mathbf{n}$ is the unit normal to the surface, with arbitrarily chosen orientation. The equation (25) has the practical implication (say for finite element calculations) that, unlike conventional plasticity, the plastic distortion field has to satisfy a "hard" partial continuity constraint, *i.e.*, the tangential action of the plastic distortion rate has to be continuous at a material surface of discontinuity. The equation (24) provides for the evolution and transport of polar dislocation densities. Through the curl of the total plastic distortion rate tensor $\dot{\mathbf{U}}_\mathbf{p}$, it couples the polar and statistical dislocation densities for the nucleation of polar dislocations. Complementing the above equations with a constitutive relation for the average dislocation velocity $\mathbf{V}$ as a function of stress and dislocation orientation, and with phenomenological evolution equations for the statistical densities involved in the conventional velocity gradient $\mathbf{L_p}$, one obtains a closed theory in the sense that it contains enough statements to derive uniquely the dynamics of stress and dislocation densities in a bounded domain from boundary and initial conditions. In particular, the direction $\mathbf{d}$ of velocity $\mathbf{V}$ is prescribed as [15]

$$\begin{aligned} \mathbf{V} &= v\frac{\mathbf{d}}{|\mathbf{d}|} \\ \mathbf{d} &:= \mathbf{b} - (\mathbf{b}.\frac{\mathbf{a}}{|\mathbf{a}|})\frac{\mathbf{a}}{|\mathbf{a}|} \\ \mathbf{b} &:= \mathbf{X}(\mathbf{T}'\boldsymbol{\alpha})\ ;\ b_i = e_{ijk}T'_{jr}\alpha_{rk}\ ;\ \mathbf{a} = \mathbf{X}(tr(\mathbf{T})\boldsymbol{\alpha})\ ;\ a_i = (\frac{1}{3}T_{mn})e_{ijk}\alpha_{jk} \end{aligned} \tag{26}$$

The definition of $\mathbf{d}$ can be approached from two points of view. In the situation when the dislocation density may not be expressed as an elementary dyad formed from a Burgers vector direction and a line direction, the definition (26) arises as a sufficient condition for pressure independence of the polar dislocation plastic strain rate and ensuring positive dissipation. The dissipation in the model can be written as

$$D = \int_B (\mathbf{X}(\mathbf{T}\boldsymbol{\alpha}).\mathbf{V} + \mathbf{T} : \mathbf{L_p}) dv \tag{27}$$

Focusing on the dissipation due to polar dislocation motion, $\mathbf{X}(\mathbf{T}\boldsymbol{\alpha}).\mathbf{V}$, and writing

$$\mathbf{X}(\mathbf{T}\boldsymbol{\alpha}) = \mathbf{b} + \mathbf{a} \tag{28}$$

where $\mathbf{b}$ is a pressure-independent term, it makes physical sense to require $\mathbf{V}$ to be in the direction of $\mathbf{b}$. However, this does not guarantee that the dissipation due to polar dislocation motion is independent of pressure and neither that $\mathbf{X}(\mathbf{T}\boldsymbol{\alpha}).\mathbf{b} \geq 0$; however subtracting the component of $\mathbf{b}$ in the direction of $\mathbf{a}$ ensures the latter fact:

$$(\mathbf{b}+\mathbf{a}).(\mathbf{b}-(\mathbf{b}.\frac{\mathbf{a}}{|\mathbf{a}|})\frac{\mathbf{a}}{|\mathbf{a}|}) = \mathbf{b}.\mathbf{b} - \frac{(\mathbf{b}.\mathbf{a})^2}{|\mathbf{a}|^2} + \mathbf{a}.\mathbf{b} - \mathbf{b}.\mathbf{a} = \mathbf{b}.\mathbf{b} - (\mathbf{b}.\frac{\mathbf{a}}{|\mathbf{a}|})^2 \geq 0 \tag{29}$$

by the Cauchy-Schwarz inequality (Pythagoras' theorem). Alternatively, a compelling mechanistic interpretation arises when $\boldsymbol{\alpha}$ may be interpreted as an elementary dyad formed from a Burgers vector direction and a line direction. Then the direction of $\mathbf{a}$ represents the direction of climb whenever $\boldsymbol{\alpha}$ represents a dislocation segment of pure edge or mixed character, and it is degenerate when $\boldsymbol{\alpha}$ is of pure screw character. Thus $\mathbf{d}$ represents the fact that mixed or edge dislocations cannot climb or cross-slip whereas screw dislocations are unrestricted in their motion.

It is perhaps insightful to evoke analogies between dislocation dynamics and eddy dynamics in turbulent flow [34]. This analogy extends to transport of polar / statistical dislocation densities, as expressed through Eqs.(18,23,24), and Large Eddy Simulations (LES) in the analysis of turbulence [18]. Turbulent flow is characterized by eddies at all scales. Averaging in space and time the Navier-Stokes equations provides equations for large resolved eddies, while unresolved ones are dealt with using additional sub-grid-scale variables. Closure of the theory is obtained through sub-grid phenomenological models featuring scaling character [35]. In dislocation dynamics, averaging in space secures equations for polar dislocations while providing the link with conventional plasticity: closure for the unresolved variables $\mathbf{L_p}$ derives from well-established models for the viscoplasticity of crystalline materials, *i.e.*, relations for forest hardening and lattice rotation having received decades of attention and experimental validation (see below Eqs.(30,31,40)). Also in contrast to turbulence, scaling behavior is associated with grid scale level, not sub-grid scale, as we show in Section 4.

Two types of solutions are offered in what follows, in order to provide various insights. First we conduct full 3-D numerical solutions of Eqs. (14-18) in single crystals, by using a Galerkin - Least Squares finite element method appropriate for transport problems (see [15, 18] for details). In these simulations, the plastic velocity gradient $\mathbf{L_p}$ follows from the activity of the statistical mobile dislocations on all slip systems

$$\mathbf{L_p} = \sum_s \rho_m b V_s \mathbf{b_s} \otimes \mathbf{n_s}, \tag{30}$$

where ρ_m is the mobile statistical dislocation density, $\mathbf{b_s}$ and $\mathbf{n_s}$ are the slip system Burgers vector and glide plane normal respectively. V_s is the ensemble dislocation velocity, which follows the power law relationship

$$V_s = V_0 sgn(\sigma_s)(\frac{|\sigma_s|}{\sigma_0 + \sigma_h})^n, \quad \sigma_s = \mathbf{b_s} \otimes \mathbf{n_s} : \mathbf{T} \tag{31}$$

Here σ_s is the resolved shear stress on a glide plane, with reference velocity V_0, athermal stress σ_0 and stress exponent as material parameters. The threshold stress σ_h reflects short range obstacle overcoming. It relates to the statistical forest density ρ_f through the usual Taylor relation $\tau_h = \alpha \mu b \sqrt{\rho_f}$, where α is a non dimensional parameter. Large n values reflect abruptness of dislocation unpinning from obstacles. The velocity V of polar dislocations is taken as the average of the statistical slip velocity absolute values $|V_s|$ over all slip systems. Hence, the same physics applies to both dislocation species. We shall also consider simplified situations with dislocations pertaining to, and gliding in a single slip plane with no out-of-plane motion. The latter simulations provide for representative behavior of some portion of a slip plane in a single crystal experiment.

3 Effects of sample size on mechanical response

In a torsion test, the shear stress increases from the axis to the exterior of the sample. When investigating the plastic response of materials, this gradient is commonly viewed as a drawback of torsion testing. It becomes beneficial when the material behavior involves internal length scales associated with emerging dislocation microstructures. The inhomogeneity of the boundary conditions then generates polar dislocations, which give rise to long-range elastic stress fields. Hence torsion is a challenging case for theories of plasticity with internal length scales. Thin copper wires with diameters in the range $12 - 170 \mu m$ were twisted in order to probe into such theories [6]. Size effects were reported, and the trend is that the greater is the imposed gradient, the greater is the degree of hardening. However, the large strains achieved, the polycrystalline character of the material, the texture evolution and varying grain size of the samples may have complicated the interpretation. In the present Chapter, the creep response of ice single crystals in torsion, a much simpler material and experimental configuration, is described with focus on the effects of the sample dimensions on this response. As an hcp material with a strong anisotropy of plasticity, ice is a choice material in this respect. It deforms plastically by the activity of basal slip systems almost exclusively [36] and it is characterized by a low Peierls stress [37]. Plastic anisotropy

and a low lattice friction favor long-range elastic interactions and dislocation transport, as well as their interactions and, indeed, the creep response of ice single crystals oriented for basal slip in torsion exhibits spectacular size effects in the *cm* range [19].

In [19], the torsion creep tests were carried out on cylindrical samples machined from laboratory grown single crystals. The applied torque M was such that the average shear stress across a sample cross section $\bar{\tau} = 3M/2\pi R^3$ (R is the sample radius) remained constant throughout the experiments. Fig.

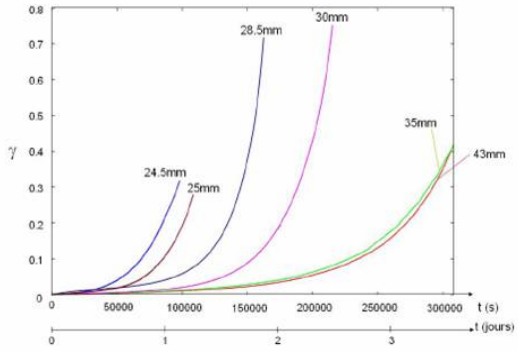

Fig. 4 Creep strain on outer surface vs. time, for various diameter values. The average shear stress is $\bar{\tau} = 0.12MPa$. In each sample, height and diameter are equal, in order to avoid any bias due to end effects. Courtesy of Juliette Chevy [38].

4 shows the forward creep curves, i.e., the evolution in time of $\gamma = \kappa R$, the strain on the outer surface ($\kappa = \theta/h$ is the constant twist per unit length of the sample). A forward and reverse creep curve, with the torque sign changed at reversal, is also shown below in Fig. 7. Dimensional analysis shows that, for a material devoid of internal length scales, creep curves gathered from samples with varying radius superpose if the average shear stress $\bar{\tau}$ and height/radius ratio are kept constant. Conversely, distinct curves in this plot are evidence for an effect of size on the plastic response. Fig. 4 suggests that the time needed to achieve a given strain decreases with the diameter, which indicates a softening effect of diameter reduction on the sample response, a trend opposite to that reported in [6] for polycrystalline Cu samples. Dispersion in the curves is existing, but limited. It results mainly from uncontrollable fluctuations in the initial dislocation microstructure, which lead to uneven initial creep strain rates.

Hard X-ray diffraction analyzes performed on slices extracted from the strained samples show that plasticity is almost exclusively due to polar dislocations of screw character gliding in basal planes, with very few mobile statistical dislocations [39]. The initial density of dislocations present in the samples, mostly sessile dislocations, was shown to be small (less than $10^8 m^{-2}$).

In addition, the analyses reveal a scale invariant arrangement of polar dislocations along the torsion axis suggesting propagation of slip in this direction. The latter can be explained by the occurrence of double cross-slip of screw dislocations through prismatic planes [40].

Interpretation in terms of dislocation dynamics of these observations is now provided on the basis of the model described in Section 2. We begin with a simplified 1-D model designed for twofold purpose: to illustrate the critical aspects of the theory; to allow for effective parametric study of size effects. In this idealization for deformation under a gradient of simple shear, we consider screw dislocation density of infinite extent in the (x_1, x_3) tangential and axial directions, line and Burgers vector along the tangential direction x_1 and transport in the radial direction x_2. The distributions of shear stress σ_{13}, polar screw density α_{11} and mobile statistical density ρ_m along a sample radius are the unknowns. The resulting equations, derived from the complete set (14-18) in creep reduce to

$$\sigma_{13,1} = \sigma_{13,3} = 0 \tag{32}$$

$$\dot{\alpha}_{11} + (\alpha_{11} v_2)_{,2} = -(\rho_m b v)_{,2} \tag{33}$$

Here b is the length of the Burgers vector, and a comma indicates a partial derivative. The shear stress σ_{13} cannot be obtained from these simplified equations, and recourse is made to approximations. Since the concern is on transient primary creep and the sample remains mostly elastic in its central part, as will be discussed below, an elastic approximation is used: $\sigma_{13} = (x_2/R)\tau$. It was checked that the latter differs from the stress distribution expected for a fully viscoplastic response by less than 15%. Eq. (33) is a transport equation. It represents the transport of screw dislocations along the radius with a source term due to gradients in statistical dislocation mobility. Account of the physics of dislocation velocity and of the history of straining is now made through phenomenological statements. Following [36], we assume a power law relationship for the average polar and statistical dislocation velocities (v_2, v) in the form

$$v_2 = v = v_0 sgn(\sigma_{13} - \sigma_\mu)(\frac{|\sigma_{13} - \sigma_\mu|}{\sigma_0 + \sigma_h})^n \tag{34}$$

with $n = 2$. Parameters (v_0, σ_0) are reference velocity and stress values, respectively. They are identified from the experimental data [36, 37]. An isotropic statistical hardening is derived from the sessile density ρ_s in the Taylor form: $\sigma_h = \bar{\alpha}\mu b\sqrt{\rho_s}$, where μ denotes the elastic shear modulus and $\bar{\alpha}$ is a constant. Only a fraction $(1 - \beta)$ of the nucleated screws glides in the basal planes. They induce a back-stress, with rate of formation

$$\dot{\sigma}_\mu = \tilde{\alpha}\mu\alpha_{11} v_2 - \frac{|v_2|}{\hat{\alpha} b}\sigma_\mu \tag{35}$$

where $(\tilde{\alpha}, \hat{\alpha})$ are constants. Relation (35) is similar to the Armstrong-Frederick law for kinematic hardening [41], but here the back-stress builds up from polar dislocation mobility only. Note that the involved relaxation time $\tau_r = \hat{\alpha} b/|v_2|$ is inversely proportional to the polar dislocation velocity. It is such that, at equilibrium ($\dot{\sigma}_\mu = 0$), the back-stress value does not depend on the dislocation velocity, but only on the polar dislocation density. The complementary fraction β of nucleated screws experiences out-of-plane motion induced by the internal stress field. Therefore the statistical sessile density increases - due to the formation of edge segments in prismatic planes, assumed to be proportional to the rate of screw nucleation

$$\dot{\rho}_s = \beta |(\alpha_{11} v_2)_{,2}| \tag{36}$$

In our calculations, σ_h remains smaller than the reference stress σ_0, implying that statistical hardening is relatively insignificant, whereas the back-stress σ_μ can be of the order of the applied stress τ. The statistical mobile dislocation density ρ_m has a very low initial value. It increases due to dislocation sources associated with edge jogs in prismatic planes [42]. Its nucleation rate is supposed to be proportional to the shear strain rate, with coefficient C_1. Saturation of mobile dislocations results from their mutual annihilation, with coefficient C_2.

$$\dot{\rho}_m = (\frac{C_1}{b^2} - C_2 \rho_m) \dot{\Gamma}, \quad \dot{\Gamma} = |\alpha_{11} v_2 + \rho_m b v| \tag{37}$$

Note that the evolution law (37) is also used in the upcoming 3-D com-

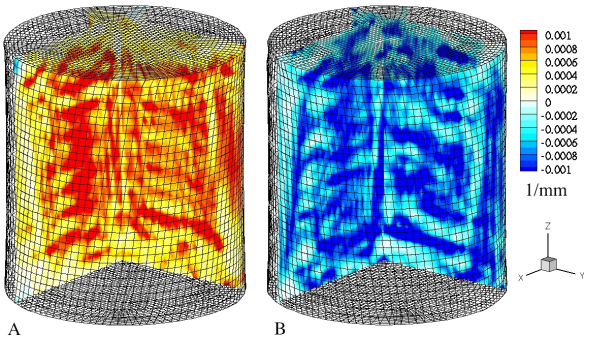

Fig. 5 Polar screws α_{11} piercing the plane with normal in the x_1 direction and α_{22} piercing the plane with x_2 normal: A) just before reversal in Fig. 7; B) the structure developed after reversing the direction of creep, at the end of the curve.

putations, with $\dot{\Gamma} = |\dot{\mathbf{U}}_\mathbf{p}|$, but that the latter automatically include out-of-plane dislocation motion and back-stress build-up. Their presence in the phenomenology of the 1-D formulation through Eqs. (35, 36) is an offset for

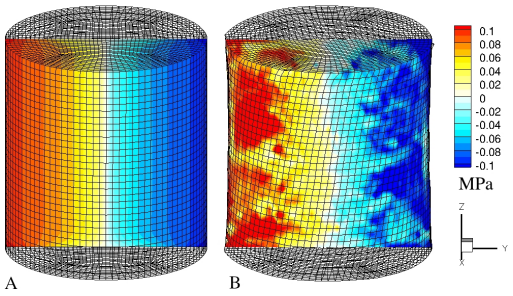

Fig. 6 Shear stress component σ_{13} shown at the beginning (A) and end (B) of the blue dashed curve in Fig. 7. The figure highlights the development of stress due to the multiplication of polar dislocations, from the (effectively) elastic solution with low mobile density. Plot A also shows end effects in the distribution of stress.

the assumed invariance in the c-axis direction. Model parameters and initial conditions are given in Table I.

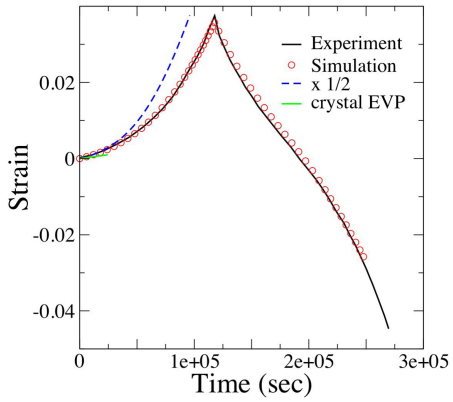

Fig. 7 Creep curves in forward / reverse torsion from experiments, 1-D and 3-D models. The blue dashed line shows the forward creep curve for a sample with halved radius and height. It is seen that the acceleration of creep increases when the sample size is reduced. The green continuous line, obtained for conventional elasto-viscoplastic (EVP) treatment, shows that the latter is unable to retrieve the acceleration of creep.

Fig. 5 shows the (locally-resolved) polar screw density and Fig. 6 the shear component of the stress obtained from the 3-D model. Note that the 3-D stress distribution supports the assumption made in the 1-D idealization. Under a positive torque, an outstanding feature of both models is the nucleation of positive screw dislocations close to the edge of the sample, their

Table 1 Numerical constants and initial conditions used in the model

b	v_0	σ_0	n	μ	β	C_1	C_2
$4.5 \times 10^{-10}m$	$3.6 \times 10^{-7}m/s$	$0.1MPa$	2	$3GPa$	0.1	10^{-8}	17
$\bar{\alpha}$	$\tilde{\alpha}$	$\hat{\alpha}$		ρ_m	ρ_s	$\alpha_{11}(R)$	
0.133	0.666×10^{-2}	10^5		10^6m^{-2}	10^8m^{-2}	$0.32m^{-1}$	

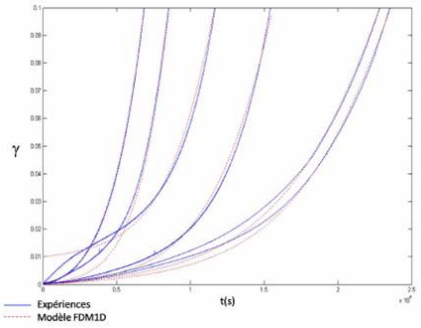

Fig. 8 Experimental data from the creep tests shown in Fig.4 and simulated creep curves from the 1-D model. In the model, initial conditions on screw dislocation density are consistent with the observed initial strain rate $\dot{\gamma}$. Courtesy Juliette Chevy [38].

transport towards its axis and, as stress and velocity decrease in this area, the formation of pile-ups. As seen in Fig. 7, the continuous increase in the forward creep rate is retrieved from both models. The reverse torsion behavior is also shown in the figure. At torque reversal, an increase in the creep rate absolute value is observed in the experiments. It is fully retrieved by both the 1-D and 3-D models. This asymmetry of slopes at the reversal point can be attributed to the positive screw dislocation pile-ups built in forward torsion. Whereas they were opposing dislocation motion in forward loading, the resulting internal stresses are helping reverse dislocation motion after torque reversal, hence the "instantaneous" creep acceleration at reversal. Screw dislocations of negative sign are nucleated in reverse loading, which progressively annihilate with the positive screw pile-ups created in forward loading. Hence, the total polar screw density decreases, with the consequence that the positive screw pile-ups are dismantled and that the creep rate absolute value decreases. The minimum creep rate value is reached at the inflexion of the creep curve. At this point, creep is mostly accommodated by statistical dislocations. In the rest of the reverse creep curve, creep keeps accelerating while negative screw pile-ups are created, in a fashion similar to forward loading, though obviously with reversed sign. Hence, the anisotropy of creep behavior derives from the nucleation, transport and annihilation of inhomogeneous polar screw density distributions. The excellent agreement between experimental and simulated creep curves suggests that these ingredients are indeed key aspects of the

physical response.

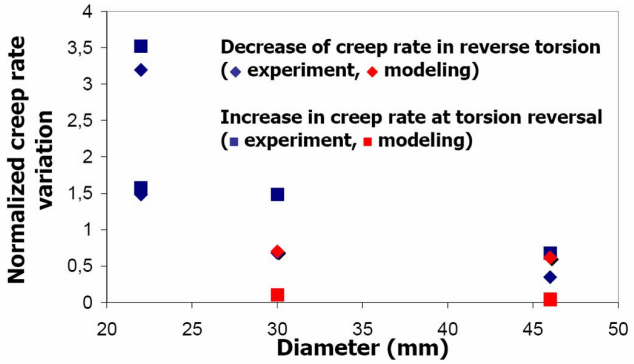

Fig. 9 Sample diameter effects on acceleration of creep rate at torsion reversal and on creep rate deceleration during reverse torsion, from reversal to inflexion of the creep curve (experimental data from creep tests in blue, data from 1-D simulations in red; experimental and simulation data coincide for the smallest diameter).

Sample size effects on the creep response are obtained. By reducing the sample diameter, screw nucleation is promoted and acceleration of the creep rate increases, in close agreement with experimental data (see Figs. 7,8). Thus, the greater is the imposed gradient, the greater is the degree of softening, not hardening as would have been expected if polar screw dislocations had been contributing to isotropic statistical hardening in a way similar to statistical dislocations. Rather, the polar screw dislocations induce softening due to larger rates of plastic distortion. Several other effects of sample size on mechanical response were predicted by the model and observed in the experiments. We report here on two such effects, observed in reverse torsion and shown in Fig. 9. Firstly, the larger is the imposed gradient (the smaller is the sample diameter), the larger is the increase in the creep rate absolute value at torque reversal. Secondly, the larger is the imposed gradient, the larger is the decrease in the creep rate, from torque reversal to inflexion of the creep curve. Note that the latter is a hardening effect on the creep response. As mentioned above, the asymmetry of the creep curve at torsion reversal reflects screw dislocation pile-ups and internal stresses built up during forward torsion. Hence, the larger is the imposed gradient, the larger are the internal stress level and creep rate acceleration at reversal. The interpretation suggested by the model for the second effect is as follows. Since the inflexion point corresponds to the instant when the polar screw density is the closer to zero, a larger deceleration in the creep rate is representative of a larger nucleation of polar screw density, which in turn is due to a larger imposed gradient.

In pure Cu, experimental evidence of sample size effects on mechanical response is still controversial. The work by Fleck et al. [6] on polycrystalline Cu seems to be pointing at response hardening when the sample diameter is reduced. However, data on Cu single crystals loaded in tension rather indicate strong decrease of hardening in the easy glide region when crystal radius is decreased [43]. We note that observations similar in spirit to ours [44] were made in order to explain the "anomalous hardening effect" observed in [6]. In this reference, the reduction in the density of polar screw dislocations in the center region of the sample is seen as the origin of hardening. As its plastic distortion is reduced near the axis, the metal behaves more like an elastic solid and, as such, it becomes harder. The difference in behavior with ice single crystals might then be attributed to the difference in the elastic constants values (the elastic shear modulus in ice is of the order of $3GPa$, much smaller than the $40GPa$ Cu value). On the basis of the above simulations, dislocation transport and long-range internal stress build-up appear as the controlling mechanisms for the rarefaction of polar screw dislocations in the center of the sample, through polar screw pile-up formation.

4 Intermittency of crystal plasticity: scale invariance and transport effects

Transport is a convective process, pervasive in many branches of physics, by which certain species, or variations in certain quantities, propagate in a medium. For example, it serves as a cornerstone in the theory of fluid dynamics. When envisioned on length scales over which areal densities of dislocations may be envisaged, dislocation motion is amenable to the transport of these densities. The fundamental equation for dislocation transport (7) has been known for half a century [12, 13], mostly as a curiosity, and only recently has it been effectively used for dislocation dynamics predictions [9]. Similarly, the relevant length scale for the observation in dislocation dynamics of the propagative features associated with transport has remained elusive, and only recently has experimental evidence been provided [26], although observation of strain waves [45] could perhaps have given a clue earlier.

An inherent connection between dislocation transport and the intermittency of plastic activity is revealed in [26] by applying high resolution extensometry to Cu single crystals in tension. When oriented for multislip, Cu single crystals represent the truly emblematic situation where material instability can be ruled out and homogeneous straining in a traditional (mechanical) sense expected at small strains (see loading curve in Fig.10). Yet, the inhomogeneous dislocation microstructure and the intermittent dislocation activity at a microscopic scale may well induce intermittency and inhomogeneity in dislocation transport at some intermediate scale. Hence Cu crystals represent the perfect case for evidencing intermittency and dislocation transport

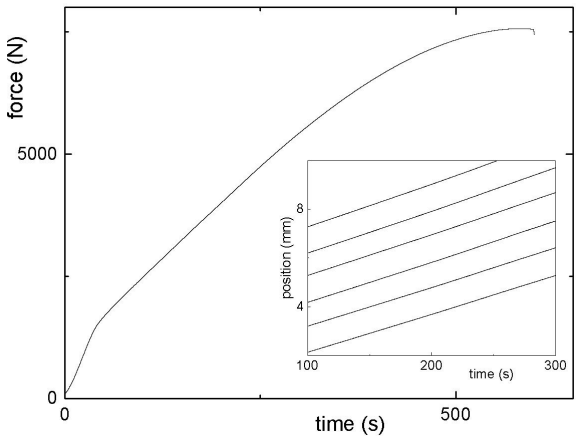

Fig. 10 Cu single crystal oriented for multislip under uniaxial tension (Gauge length: $30mm$, width: $5.5mm$, thickness: $5.5mm$, Schmid's factor: 0.3, temperature: $20C$, driving strain rate: $\dot{\epsilon}_a = 5 \times 10^{-4} s^{-1}$), macroscopic force vs. time (main graph) and displacement vs. time in six locations distant by $1mm$ (inset).

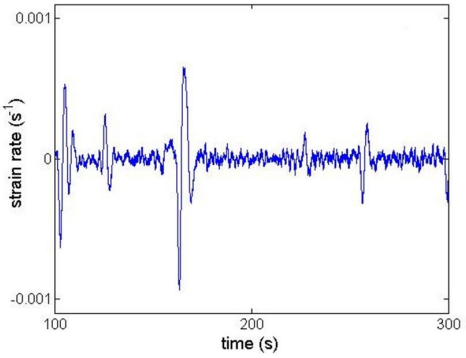

Fig. 11 Variations of axial strain rate about the driving strain rate $\dot{\epsilon}_a == 5 \times 10^{-4} s^{-1}$, as obtained from the lowest displacement curves in the stack in Fig. 10. Note that the maximum size of the fluctuations $2.5 \times 10^{-3} s^{-1}$ is much larger than $\dot{\epsilon}_a$.

properties. The extensometry method is based on a digital image correlation technique in one-dimensional setting. The sample surface is painted with alternated black and white strips, which perfectly reflect the material displacement underneath. A high resolution CCD camera with recording frequency $10^3 Hz$ and pixel size $1.3\mu m$ captures the longitudinal displacements of the black - white switches, from which the axial strain rate field is rendered. Subtracting the constant driving strain rate $\dot{\epsilon}_a$ from the local strain rate at

a material point leaves the variations shown in Fig.11. Despite smoothness of the loading curve in Fig.10, Fig.11 displays jerks well above experimental noise level. The figure suggests that the intermittency of dislocation motion at the microscopic scale shows up at a somewhat larger scale. The probability density for the size of jerks in Fig.11 shows power law scaling (see Fig.12), with scaling exponent $\tau \approx 2$. This exponent is consistent with the

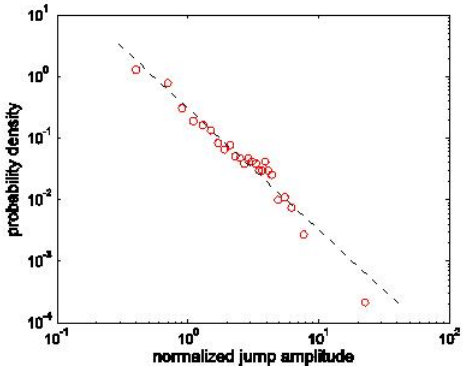

Fig. 12 Probability density (normalized to bin size) for event size in the time series shown in Fig.11. The dashed line indicates the power-law trend with slope $\tau = 2$.

scaling law reported for the associated acoustic emission [25]. Such scaling is evidence for self-organization of the observed fluctuations, which is also demonstrated by Fig.13. The figure features a space-time diagram for local fluctuations about the driving strain-rate during the elasto-plastic transition in the test shown in Fig.10. It displays spots of intense activity dotted along straight lines, suggesting wave propagation at constant average speed. The average wave velocity measured from the slope of the characteristic lines (about $10^{-2} m.s^{-1}$) is five orders of magnitude smaller than the velocity of elastic waves, but much larger than the material particles velocity. It is of the order of the average velocity of dislocation ensembles, which suggests that the observed waves reflect the underlying collective motion of dislocations. In this interpretation, the dotted pattern of spots along the characteristic lines is manifestation of the intermittency of collective dislocation motion. It is also proof to the wavy structure of plastic activity, when envisioned at appropriate length scale. At larger strains, this wavy pattern is seen on shorter time and length scales, because the dislocation mean free path decreases in relation with the multiplication of forest obstacles.

A 3-D generic simulation of the above experiments using field dislocation dynamics is now briefly outlined. The reader is referred to [26] and [46] for further details. A flat Cu whisker is clamped to the left end, while the right end has constant velocity. The applied strain rate is $\dot{\epsilon}_a = 10^{-3} s^{-1}$. The elas-

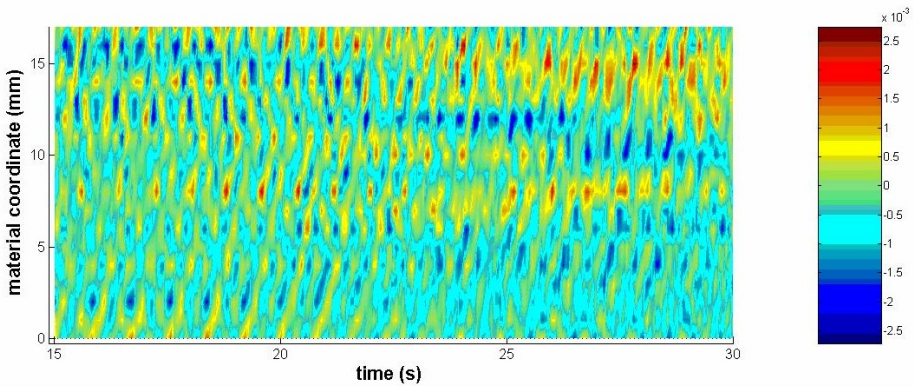

Fig. 13 Longitudinal fluctuations about the imposed strain rate in a space - time diagram during the elasto-plastic transition. Dotted characteristic lines run from the left and right of the gauge length, reflecting intermittency and transport. The imposed strain rate is $\dot{\epsilon}_a = 5 \times 10^{-4} s^{-1}$. Fluctuations can be as high as $2.5 \times 10^{-3} s^{-1}$.

tic response is taken to be anisotropic with constants C_{11}, C_{12} and C_{44}, and the evolution equations for ρ_m and ρ_f are

$$\dot{\rho}_m = (C_1/b^2 - C_2\rho_m)\dot{\Gamma} \tag{38}$$

$$\dot{\rho}_f = (C_0 b|\boldsymbol{\alpha}| + C_2\rho_m)\dot{\Gamma} \tag{39}$$

as outlined in [47], with simplifications deemed appropriate for the low strain level achieved in the experiments. C_0, C_1 and C_2 are material parameters accounting for the interaction between polar and forest dislocations, the mobile dislocation generation and loss, respectively. The material parameters are listed in Table 2. Note that there is no inhomogeneity introduced in either the material parameters or the initial conditions.

Table 2 Material parameters used in the $3D\ Cu$ whisker simulation.

α	b	n	V_0	σ_0	
0.35	$2.5 \times 10^{-10} m$	20	$3.5 \times 10^{-8} m/s$	$3.7 MPa$	
C_0	C_1	C_2	C_{11}	C_{12}	C_{44}
25	$2.43\ 10^{-5}$	3.03	$170 GPa$	$123 GPa$	$75.2 GPa$

Elastic loading of the sample is followed by a yield drop associated with plastic activity localized near the clamped end, then by a stress plateau shown in Fig.14. Thus, inhomogeneity of plastic straining clearly stems from the inhomogeneity of the boundary conditions. This prediction of a yield drop is in full agreement with experimental data on Cu whiskers [48, 49, 50]. During

the plateau, the plastic activity propagates along the sample through the motion of a plastic front, before linear homogeneous strain hardening takes place. Propagation does not occur in this flat sample if transport is turned off in the equations. For further details on the propagation of slip along the plateau, the reader is referred to [46]. Here, we focus on the intermittency of plastic activity during the eventual linear hardening period. Bursts in stress -

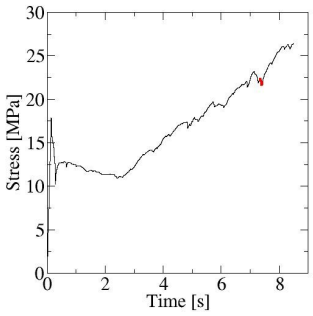

Fig. 14 Simulation of the tensile test of a flat Cu whisker of dimensions $200\mu m \times 30\mu m \times 2400\mu m$; stress vs. time response during the elasto-plastic transition and stage II linear hardening. The highlighted portion corresponds to the strain rate plots shown in Fig.15

rate are seen all along the curve during this period. Statistical analysis of the stress rate shows power law scaling with exponent $\tau = 1.9 \pm 0.1$ in the burst size distribution, consistent with the experimental data reported in [26] and in Fig.12. One particular sequence, highlighted in Fig.14, corresponds to the plots of plastic strain rate shown in Fig.15. In this figure, intermittent events and transport are clearly seen, with a general progression of plastic activity from left to right of the sample.

In view of these results, $2D$ simulations (of course more tractable than $3D$) were carried out in order to check for scaling behavior at a smaller scale and for possible variation of the scaling exponent under diverse material and experimental conditions. In these simulations, a rectangle subjected to constant shear rate $v_{1,3}$ at boundaries is considered in a glide plane of a Cu single crystal. Only dislocations pertaining to, and gliding in this plane are considered. Out of plane motion by cross-slip and climb is not considered, and single slip activity is assumed. As all gradients normal to the slip plane are ignored, out-of-plane features of lattice incompatibility and internal stresses are lost in this simplified description. Elasticity is taken to be isotropic with shear modulus μ. The average velocity V of dislocations in the plane is described with the thermally activated constitutive law

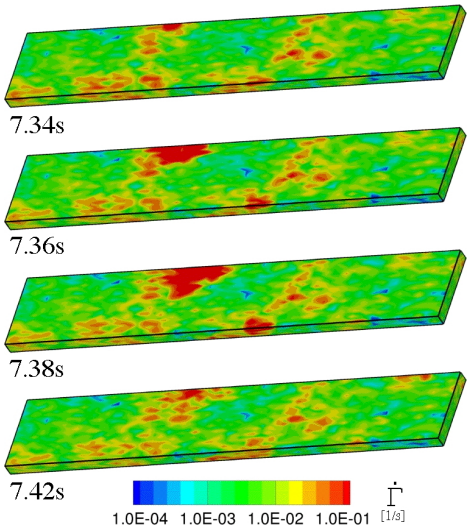

Fig. 15 Successive frames of the strain-rate spatiotemporal field along the sample showing intermittent plasticity through dislocation transport, and general progression of plastic slip from left to right. The sequence highlights a single plastic burst shown in Fig14.

$$V = V_0 exp\frac{-\Delta G_0}{kT} exp(\frac{V^* \sigma_s}{kT(1+\sigma_h/\sigma_0)}) \tag{40}$$

where V_0 is a reference velocity, $(\Delta G_0, V^*, k, T)$ a reference enthalpy, the activation volume, the Boltzmann constant and the temperature. σ_s is again the resolved shear stress and σ_h the threshold stress for obstacle overcoming. Eq.(40) is an alternative to Eq.(31), used to describe weak rate-sensitivity of the shear stress.

Table 3 Initial and boundary conditions, complementary material parameters in $2D$ simulations

$\alpha_{ij}(0)$	$\rho_m(0)$	μ	σ_h	$v_{1,3}$	kT/V^*
0	$10^8 m^{-2}$	$40GPa$	$50MPa$	$5\times10^{-4}s^{-1}$	$2.27MPa$

The imposed strain rate is $\dot{\epsilon}_a = 5\times10^{-4}s^{-1}$. In the initial configuration, polar dislocations are absent and the statistical mobile density is chosen at random about an average value. Since the boundary conditions are homogeneous (in contrast to the above 3D simulation), the incompatibility arising from the distribution of statistical dislocations is initially the only source for polar dislocations. The information on material parameters, initial and boundary conditions is summed up in Table 3.

Fig.16 shows a space-time diagram for the strain-rate fluctuations. In qual-

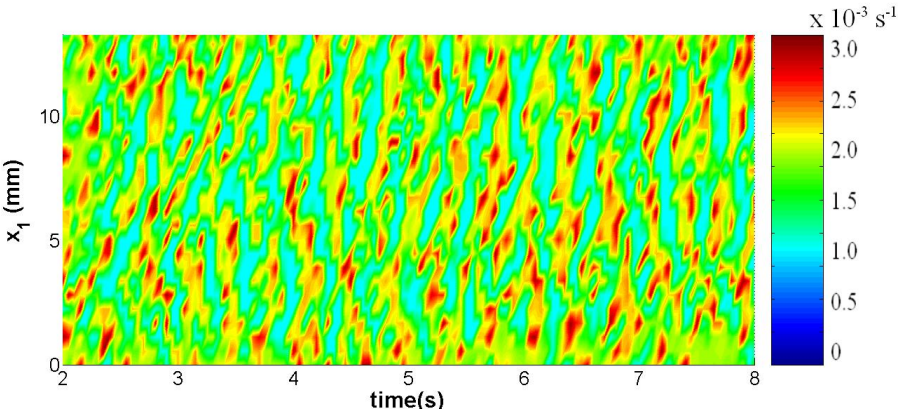

Fig. 16 Model predictions for axial (x_1) strain-rate fluctuations in a space - time diagram. The sample is a $13mm \times 13mm$ square in a glide plane subjected to equal shear rates $5 \times 10^{-4} s^{-1}$ on both sides. The figure shows the evolution in time of the strain rate profile seen along the x_2 direction.

itative agreement with Figs.13 spots of intense plastic activity dotted along straight lines are seen. This pattern follows naturally from the development of polar dislocation density, by virtue of dislocation transport and internal stress. The velocity obtained from the slopes in Fig.16 has the order of magnitude observed in experiments. Fig.17 shows the probability density for event size computed from the time series obtained for the net shear strain rate at several material points in the plane. A scaling distribution is seen, with exponent $\tau \approx 2$ in agreement with both the exponent found from the stress vs. time response and the experimental value. This result confirms that the fluctuations in Fig.16 are not numerical noise, but reflect instead correlations due to polar dislocation development, long-range stress and dislocation transport.

As reported in [26], the statistics of intermittency, and in particular the exponent value $\tau \approx 2$, seem to be insensitive to sample size and shape, or to the driving strain rate, to the extent that velocity gradients remain large enough to induce polar dislocation development, however. With unchanged geometry and loading conditions, possible influence of material behavior was also investigated by switching from a thermally activated law in Cu (Eq.(40) with material parameters in Table 3) to viscous drag in ice (Eq. (31) with material parameters from Table 4) in the simulations. Despite these differences, a scaling regime with exponent $\tau \approx 2$ in the event size distribution is still found. Thus, the scaling behavior of intermittency obtained from the model features a rather universal scaling exponent. In the interpretation suggested

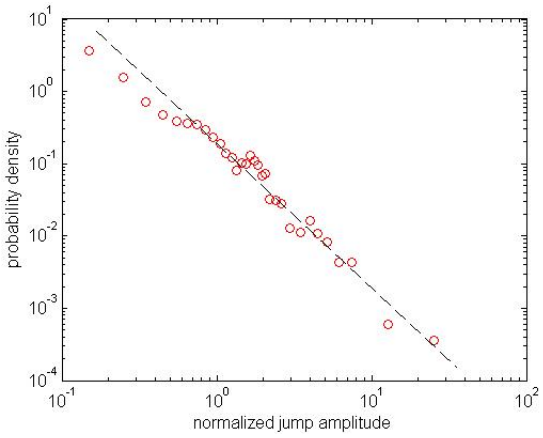

Fig. 17 Probability density of event size in a 2-D simulation. The event size is defined as the maximum strain rate value during the event. The dotted line shows a $\tau = 2$ slope.

by the present model, intermittency of plastic activity requires abruptness of the unpinning transition on short range obstacles as described through the weakly rate-sensitive stress-velocity relationships (31, 40) at the present scale of resolution. The model implies that both dislocation transport and long-range interactions play a role in the emergence of the scale-invariant behavior of intermittency. As dislocation transport involves such mechanisms as double cross-slip of screw dislocations by-passing short-range obstacles, it follows from this remark that short-range interactions play a significant role in the intermittency of plastic activity. Such a conclusion is fully consistent with the observations of dislocation avalanches arrested on obstacles made in dislocation dynamics simulations [30].

5 Internal stresses and anisotropy of mechanical behavior

The sharp yield point phenomenon [51, 52] primarily occurs in b.c.c. polycrystals at room temperature. In a tensile sample loaded at constant crosshead velocity, it is associated with a band of localized dislocation activity, the so-called Lüders band, travelling along the sample. The band nucleation, usually at one grip, corresponds to a drop in stress, from the Upper Yield Point (UYP) to the Lower Yield Point (LYP). The plastically strained area then spreads along the sample. A clear cut front separates this area from the unstrained one, into which it propagates, until the sample is uniformly stretched. From this point (referred to as the Lüders strain) onwards, the

deformation proceeds uniformly in the sample. It is commonly accepted that strain aging is responsible for this behavior: solute atoms tend to diffuse to arrested dislocations, which increases the unpinning stress up to the UYP level. Dislocations are collectively unpinned at the UYP, but since the stress needed to accommodate the imposed strain rate is substantially lower, an abrupt multiplication of dislocations takes place, along with elastic relaxation of the rest of the sample. This unpinning mechanism has intricate connections with the spatial correlations responsible for band propagation. According to the Cottrell assumption [53], propagation occurs once stress concentration due to dislocation pile-ups at grain boundaries is able to activate new dislocation sources in neighboring grains. The long-range internal stresses due to incompatibilities in plastic strain in the vicinity of the band provide the mechanism for band propagation.

In a low-carbon steel, evidence of the role of internal stresses in the unpinning mechanism is also provided by the directionality of the yield point. If such a material is deformed beyond the Lüders strain, then aged and further strained, a sharp yield point phenomenon reappears provided straining is pursued in the same direction. Such a behavior can be explained within the framework of a local model coupling aging properties with isotropic strain hardening [54]. However, if the sample is strained in the direction opposite to that before aging, a Baushinger effect is observed and the sharp yield point phenomenon is usually absent [55, 56, 57]. This phenomenon is shown in the tension - compression of a mild steel in Fig. 18. Such directionality of the yield

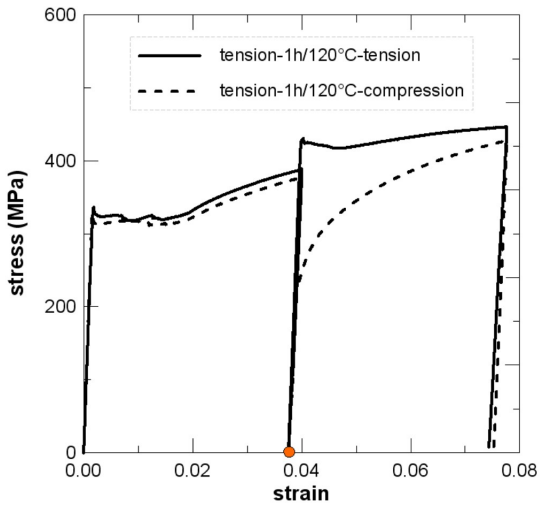

Fig. 18 Stress - strain curves during tension - aging - tension and tension - aging - compression experiments on a 1020 mild steel. The aging period is marked with an orange dot. For convenience the sign of the compression stress is reversed. Both tension and compression stresses are plotted against the same cumulative strain.

point is of considerable practical importance. It may be useful, as it curbs the return of the sharp yield point in temper-rolled or bake-hardened steels, but it may also limit the benefits of strain aging as a strengthening mechanism. Further, it demonstrates that the strain aging and unpinning mechanisms are dependent on the gradients of the distribution of dislocations, which challenges local interpretations. In the present Chapter, an interpretation of the yield point directionality is presented by using the framework of a field dislocation dynamics model. We strive to understand this phenomenon by coupling the evolution of polar and statistical dislocations with the kinetics of strain aging [27].

The model for strain aging is developed and applied to pure torsion in order to set up the simplest possible configuration. In parallel, the model is also used in a three dimensional approach, with some minor variations to be indicated below. In using the pure torsion model, the goal is to provide heuristic modeling, fit for the illustration of the critical aspects of the approach, *i.e.*, the connections between strain aging and dislocation microstructures. The unique active slip plane, $(\mathbf{e_1}, \mathbf{e_2})$, is assumed to be normal to the torsion axis. It is also assumed that plastic strain is accommodated by "circumferential" screw dislocations of infinite extent in the $\mathbf{e_1}$ direction only. For a positive torque, positive screw dislocations move from the edge of the sample toward its axis, with velocity v_2 along the radial direction $\mathbf{e_2}$. A radial screw density along the $\mathbf{e_2}$ direction does exist, in order to verify equilibrium [44], but it does not contribute to torsion accommodation. Hence it is ignored all together. The basic equations then reduce to

$$\dot{\sigma}_{13} = \mu(v_{1,3} - \rho_m b v - \alpha_{11} v_2) \tag{41}$$

along with Eqs.(32,33). Eq. (41) expresses the shear stress rate in the glide plane as a function of polar screw and statistical dislocation mobility, with μ denoting the elastic shear modulus. Account of the physics of dislocation velocity, strain aging and straining history is now made through phenomenological statements. An Arrhenius dependence is assumed for the polar and statistical dislocation velocities (v_2, v) in the form

$$v_2 = v = V_0 exp((|\sigma_{13}| - \sigma_\mu sgn(\sigma_{13}) - \sigma_h - \sigma_s)/S_0) \tag{42}$$

Here V_0 is a reference velocity, S_0 denotes the strain rate sensitivity of the flow stress in the absence of solute effects, and the numerator in the exponential represents an effective stress for dislocation glide. The reference velocity is taken in the form $V_0 = \nu_0 \rho_f^{-1/2}$, where ν_0 is a constant reference frequency for dislocation unpinning. Hence, the current waiting time $t_w = \rho_f^{-1/2}/v$ of dislocations on their obstacles is

$$t_w = \nu_0^{-1} exp(-(|\sigma_{13}| - \sigma_\mu sgn(\sigma_{13}) - \sigma_h - \sigma_s)/S_0) \tag{43}$$

In this relation, ν_0^{-1} appears as the waiting time under zero effective stress. Further, during elasto-plastic loading, t_w evolves as a function of stress, from its initial (large) value to its current, much smaller value. σ_μ is the back-stress (or internal stress), σ_h represents statistical hardening and σ_s is the additional stress due to solute hardening. The back-stress is induced by the polar screw density, with rate of formation provided by Eq.(35). Although it is an offset for the assumed invariance in the other two directions, the phenomenological treatment of the internal stresses in the $1-D$ model provides a result of general utility, *i.e.*, specific insight into the constitutive specification of back-stress evolution, to be contrasted with the Armstrong - Frederick kinematic hardening specification [41]. Isotropic statistical hardening is assumed in the Taylor form: $\sigma_h = \bar{\alpha}\mu b\sqrt{\rho_f}$, where $\bar{\alpha}$ is a constant. The evolution of statistical mobile and forest densities follows the Kubin-Estrin model [58]

$$\dot{\rho}_m = ((C_1/b^2) - (C_3/b)\sqrt{\rho_f}\,)\dot{\Gamma} \tag{44}$$

$$\dot{\rho}_f = ((C_0/b) \mid \underline{\alpha} \mid + (C_3/b)\sqrt{\rho_f} - C_4\rho_f)\dot{\Gamma} \tag{45}$$

where C_1 stands for the multiplication of dislocation line, C_3 represents mobile dislocation immobilization and C_4 dynamic recovery. The term C_0 added to the model stands for the contribution to statistical hardening of polar dislocations, through pile-ups at grain boundaries [59]. Following [60], the additional stress due to aging is expressed as

$$\sigma_s = f_0(1 - exp(-(t_a/\tau)^{2/3})) \tag{46}$$

where t_a denotes the aging time, τ is a characteristic time for solute diffusivity and f_0 represents the maximum pinning stress. The exponent $2/3$ stands for bulk diffusion, but other types of pinning kinetics could be considered as well [54]. The evolution of the aging time follows that of the waiting time with some delay, because solute concentration cannot change instantly. Following [61], these circumstances are described by allowing the aging time to relax to the current waiting time according to the first order kinetics

$$\dot{t}_a = 1 - t_a/t_w \tag{47}$$

Computation of the solutions to Eqs.(41-47) uses numerical constants provided in Table 4 (see justifications in [27]). The $3-D$ simulations also use the statistical and solute hardening modeling shown above in Eqs.(44-47), though written in terms of slip system strength and resolved shear stress. Slip system geometry is taken for bcc crystal symmetry. As development of the back-stress is inherent in the 3-D calculations, the form of the kinetic relation, Eq.(43), is also different; a constant athermal strength replaces the signed back-stress σ_μ and a constant reference velocity v_0 is used. The boundary conditions are written in terms of dislocation fluxes. Inward flux of dislocations is not permitted, although dislocation sources on boundaries are allowed. Outgoing of dislocations is permitted without constraint. The initial conditions are

Table 4 Numerical constants used in the model

b	ν_0	S_0	μ	$\bar{\alpha}$	$\tilde{\alpha}$	$\hat{\alpha}$
$2.7 \times 10^{-10} m$	$8.5 \times 10^8 s^{-1}$	$2.27 MPa$	$80 GPa$	0.3	150	10^3
f_0	τ	C_0	C_1	C_3	C_4	
$40 MPa$	$10^6 s$	25	1.45×10^{-4}	5.4×10^{-2}	20	

Table 5 Initial conditions

ρ_m	ρ_f	α_{11}	σ_{13}	t_a
$10^{12} m^{-2}$	$10^{11} m^{-2}$	0	0	$2 \times 10^6 s$

summed up in Table 5. Note that the initial distribution of dislocations is chosen to be uniform, with no polar dislocations. The initial aging time reflects saturation of dislocations with solute atoms.

Tension - compression tests were simulated using the full $3-D$ model. A polycrystal of dimensions $2mm \times 2mm \times 10mm$ was clamped to the left end, while the right end was submitted to constant velocity. The sample was first deformed in tension until the strain reaches 0.04, then unloaded. Each element was assigned a single crystallographic orientation taken from the sampling of a uniform distribution. The results are shown in Figs.(19,20).

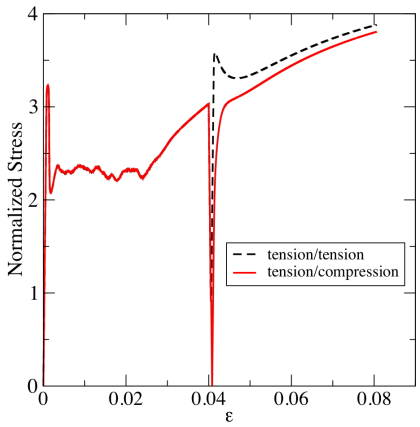

Fig. 19 Stress (normalized by the initial slip system strength) vs. strain curves in tension - aging - forward tension and tension - aging - compression $3-D$ simulations. The applied strain rate is $6 \times 10^{-5} s^{-1}$. For convenience the stress sign is reversed in compression.

An UYP associated with dislocation unpinning and multiplication is seen in Fig.19, followed by a Lüders plateau corresponding to the propagation of a band in equivalent plastic strain rate from the left end to the right end of the sample. A realistic rendering of the band is achieved, as shown in Fig.20. In this figure, the band is at angle with both the axial direction and the

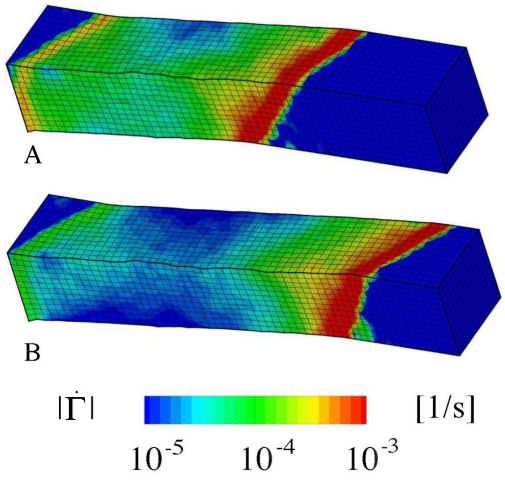

Fig. 20 Strain rate contours for the Lüders band corresponding to the stress plateau in Fig.19 at two instants A, B. After nucleation to the left, the band propagates to the right end of the sample. Note the inclination of the band, at angle with both the axial and transverse directions.

transverse direction, consistent with experimental observations in $CuAl$ and $CuMn$ single crystals [62]. The figure also shows a trailing amount of residual strain rate left behind the band. When the band reaches the right end, the sample is uniformly stretched at the Lüders strain, and deformation proceeds uniformly. At unloading, aging of the material is carried out by augmenting the aging time. When from this point, the sample is loaded forward in tension, restoration of an UYP is predicted, though strain localization is hardly seen, whereas the UYP is missing if compression is applied. In the latter case, a Baushinger effect is also predicted, as well as a transient inflexion in strain hardening. Fig.19 shows qualitative agreement with the experimental trend in mild steel seen in Fig.18.

We now proceed with simulations using the $1-D$ model to reveal the interplay between evolution of polar density, back-stress and aging. A thin walled tube is first strained in forward torsion with a positive torque until the shear strain reaches 0.04, then unloaded. An UYP is obtained, as can be seen in Fig.21. Since axial invariance is assumed and only dislocation transport in the plane normal to the torsion axis is considered, Fig.21 does not feature a Lüders plateau. Indeed, the latter goes with axial band propagation. Dislocation unpinning and multiplication shift from the outer edge, where the stress is high, to the interior where it lessens, which generates gradients in plastic strain rate. These gradients act as sources for polar dislocations. As the torque is positive, positive screws are nucleated, and a back-stress associated with these dislocations builds up. At unloading, aging of the material is per-

formed as detailed above in $3-D$ computations. When, from this point, the sample is loaded in forward torsion, restoration of an UYP is again predicted, whereas it is absent if the sense of torsion is reversed. A strong Baushinger effect is also seen in that case. The interpretation derives from the evolution of the polar screw density and back-stress shown in Fig.(22). Indeed, the back-stress opposes unpinning of aged dislocations in forward torsion because it lowers the effective stress and the dislocation velocity. Thus an UYP is needed for unpinning, but the drop in stress is reduced with respect to its first occurrence due to the concomitant reduction in the multiplication rate. In contrast, the back-stress favors unpinning and dislocation multiplication in reverse torsion, because it enhances the effective stress and the dislocation velocity. Hence, an UYP now becomes unnecessary for unpinning.

Dislocation re-arrangement and back-stress relaxation eventually play a piv-

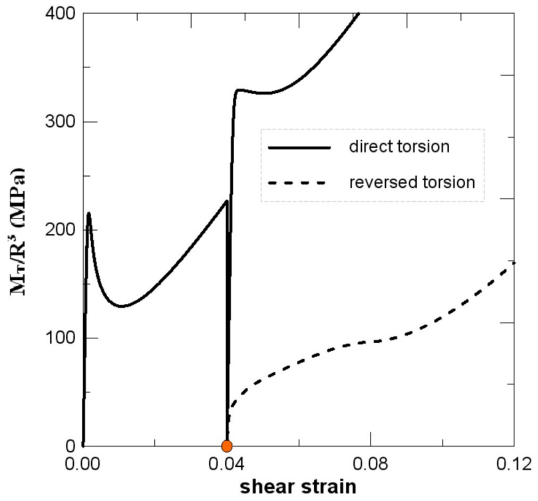

Fig. 21 Torque evolution during forward torsion - aging - forward torsion and forward torsion - aging - reverse torsion simulations. The aging period is marked with an orange dot. For convenience the torque sign is reversed in reverse torsion. Both forward and reverse torque are plotted against the same cumulative strain.

otal role. During reverse torsion, gradients in the plastic distortion generate negative polar screw dislocations, which annihilate with positive screws formed in forward torsion. Hence the total screw density and the associated back-stress drop down to zero. This drop in back-stress gradually hardens the material because it limits the dislocation velocity as well as the rate of multiplication of mobile dislocations. The dependence of the relaxation time τ_r on the dislocation velocity is such that back-stress relaxation is initially fast, and that it slows down as it comes to an end. If reverse torsion is further pursued to larger strains, a new structure of negative polar screw dislocations devel-

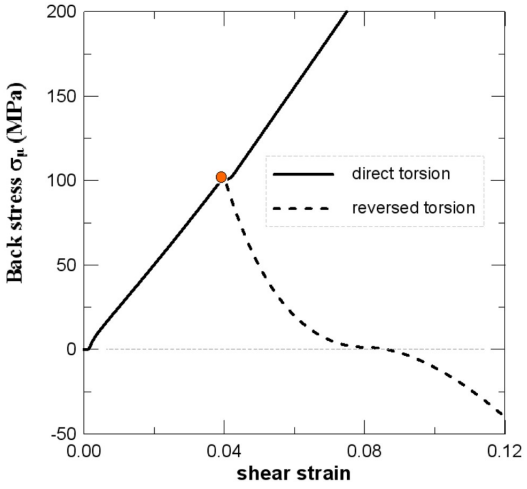

Fig. 22 Back-stress evolution during forward torsion - aging - forward torsion and forward torsion - aging - reverse torsion simulations. The aging period is marked with an orange dot.

ops and an inflexion of the (now negative) back-stress is obtained (Fig.22). This inflexion transfers to the torque history, which therefore shows transient curbing of strain hardening after path reversal (Fig.21). As mentioned earlier, this feature is also apparent in Fig.19 from tension - aging - compression $3-D$ simulations. It is consistent with observations of a similar transient behavior in polycrystalline aluminum samples at various temperatures [63] and in IF-steels when the strain path is reversed [64]. The microstructural analyses and qualitative arguments provided in these references, i.e., the annihilation of the structure of polar dislocations formed in pre-deformation and the development of a new structure along the eventual strain path, are in full agreement with our own interpretations.

6 Conclusions

Conventional plasticity is rather ineffective in the understanding of the directionality of the yield point, because it does not deal with long-range internal stresses. Arguably, conventional kinematic hardening as expressed by the Armstrong-Frederick law for back-stress evolution, has an ability to phenomenologically describe anisotropic hardening. However, spatial correlations due to the lattice distortion and internal stress fields are missed, which must have implications on back-stress build up. In contrast to standard plasticity treatment, the 3-D field dislocation model provides for polar dislocation mi-

crostructure and internal stress field development, and it naturally features induced anisotropic hardening. The formulation of the heuristic 1-D model provides insight into a more adequate specification of back-stress evolution in terms of polar dislocations through the constitutive equation (35). Phenomena related to strain path dependence of strain hardening (such as the inflexion in strain hardening after path reversal in strain-aged steels or the inflexion of creep of ice single crystals in reverse torsion) can only be retrieved from the nucleation, transport and annihilation of polarized dislocation distributions. Conventional local treatment using statistical dislocations, whose multiplication mechanisms are unaffected by strain path orientation reproduce such phenomena only by having recourse to multiple dislocation species and algorithmic rules [65]. The present model also deals separately with dislocation density and dislocation velocity, which, in contrast, are merged into plastic strain rate in standard plasticity treatment. This feature proves to be useful in the understanding of the directionality of hardening, because back-stress relaxation effects on dislocation velocity and dislocation density appear to be very much involved. It is consistent with common material science practice, which provides material data in terms of dislocation velocity and density.

The prediction of the propagation of plastic fronts has been a long-time goal of the theory of plasticity. However, its realization has been hampered by the mathematical structure of the traditional approach. Within the latter, propagating fronts of plastic deformation can be obtained only in the presence of spatial inhomogeneity in material properties (see for example [66] for the propagation of Portevin - Le Chatelier (PLC) bands in polycrystals), or when spatial coupling due to 3-D stress field equilibrium is strong enough (see [67] for the study of neck propagation in polymers). In contrast, in the presence of spatially homogeneous material characteristics or when the 3-D character of the stress field is weak (in 1-D situations or in flat samples), the capability of the field dislocation dynamics framework in representing propagating plastic fronts derives from the description of transport through partial differential equations. Then, inhomogeneity in boundary conditions may or may not trigger the propagation of plastic fronts depending upon material behavior, as illustrated by a study of PLC band propagation in single crystals [68]. Because they feature correlations in space due to both the long-range internal stresses and the short-range interactions involved in dislocation transport, field dislocation dynamics theories also provide interpretation for the scale-invariant intermittency of dislocation transport. Size effects derive as well from the presence of material length scales linked with long-range stresses and dislocation transport.

In the formulation of a mesoscopic theory, the linear dimension of the support $\Omega(\mathbf{x})$ for spatial averaging (see relation (13)) is arbitrarily chosen. Hence, flexibility is left in the order of magnitude of the spatial resolution sought for the model. Depending on the objectives of modeling, the formulation can

span from a physical theory with a short resolution length scale, where only a small number of dislocations is involved in the averaging procedure, to engineering codes applying to large scale systems, where blurring of dislocation ensembles needs to be more extensive due to computational costs. Hence, as mentioned earlier, phenomena deemed "nonlocal" in the former approach may be labelled "local " in the latter. However, if the resolution length scale is kept small enough and can be compared with the linear characteristic length of the relevant dislocation microstructures, length-scale dependence of the results can be retained.

Acknowledgments. AA gratefully acknowledges the support from the National Science Foundation through the CMU MRSEC, grant no. DMR-0520425, the LMA-CNRS, Marseille and the Dept. of Civil and Env. Engineering at CMU. AB received support under US Dept. of Energy grant DEFG03-02-NA00072 and the Center for Simulation of Advanced Rockets at the University of Illinois at Urbana-Champaign (UIUC), US DOE subcontract B341494. AB and CF benefited from exchanges under a joint agreement between Centre National de la Recherche Scientifique and UIUC. We thank Juliette Chevy for providing Figs.4,8.

References

1. L.P. Kubin, C. Fressengeas and G. Ananthakrishna, *Collective Behaviour of Dislocations in Plasticity*, in Dislocations in Solids, vol 11, Eds. F.R.N. Nabarro and M.S. Duesbery, Elsevier Science B.V., 100-192 (2002).
2. M. Legros, A. Jacques and A. George, Mat. Sci. Eng. A **387-389**, 495 (2004).
3. M. Neubert and P. Rudolph, Prog. Cryst. Growth Charact. Matr., **43**, 119 (2001).
4. M. Zaiser, Adv. Phys. **55**, 185 (2006).
5. E.C. Aifantis, Mat. Sci. and Eng., **81**, 563 (1986).
6. N.A. Fleck, G.M. Muller, M.F. Ashby and J.W. Hutchinson, Acta Metall. Mater., **42**, 475 (1994).
7. W.D. Nix and H. Gao, J. Mech. Phys. Solids, **46**, 411 (1998).
8. F. Forest, G. Cailletaud and R. Sievert, Arch. Mech., **49**, 705 (1997).
9. A. Acharya, J. Mech. Phys. Solids, **49**, 761 (2001).
10. J.F. Nye, Acta Metall., **1**, 153 (1953).
11. E. Kröner, Erg. Angew. Math,**5**, 1-179 (1958).
12. T. Mura, Phil. Mag., **89**, 843 (1963).
13. A.M. Kosevich, *Crystal dislocations and the theory of elasticity*, in Dislocations in Solids, Ed. F.R.N. Nabarro, North-Holland, Amsterdam, 33-141 (1979).
14. E. Kröner, *Continuum theory of defects*, in Physics of Defects, Ed. R. Balian et al., North Holland, Amsterdam, 218-314 (1980).
15. A. Acharya and A. Roy, J. Mech. Phys. Sol., **54**, 1687 (2006).
16. A. Roy and A. Acharya, J. Mech. Phys. Sol., **53**, 43-170(2005).
17. A. Roy and A. Acharya, J. Mech. Phys. Sol., **54**, 1711-1743(2006).
18. S. Varadhan, A.J. Beaudoin, A. Acharya and C. Fressengeas, Modelling Simul. Mater. Sci. Eng. **14**, 1 (2006).
19. V. Taupin, S. Varadhan, J. Chevy, C. Fressengeas, A.J. Beaudoin, M. Montagnat and P. Duval, Phys. Rev. Lett., **99**, 155507 (2007).

20. R. Becker and E. Orowan, Z. Phys. **79**, 566 (1932).
21. J. Weiss and J.R. Grasso, J. Phys. Chem. **101**, 6113 (1997).
22. M.C. Miguel, A. Vespignani, S. Zapperi, J. Weiss and J.R. Grasso, Nature (London) **410**, 667 (2001).
23. D.M. Dimiduk, C. Woodward, R. LeSar and M.D. Uchic, Science **312**, 1188 (2006).
24. S. Brinckmann, J.Y. Kim and J.R. Greer, Phys. Rev. Lett. **100**, 155502 (2008).
25. J. Weiss, T. Richeton, F. Louchet, F. Chmelik, P. Dobron, D. Entemeyer, M. Lebyodkin, T. Lebedkina, C. Fressengeas and R.J. McDonald, Phys. Rev. B. **76**, 224110 (2007).
26. C. Fressengeas, A.J. Beaudoin, D. Entemeyer, T.Lebedkina, M. Lebyodkin, and V. Taupin, Phys. Rev. B, **79**, 014108 (2009).
27. V. Taupin, S. Varadhan, C. Fressengeas and A.J. Beaudoin, Acta Mater., **56**, 3002 (2008).
28. M. Koslowski, R. LeSar and R. Thomson, Phys. Rev. Lett. **93**,125502 (2004).
29. F.F. Csikor, C. Motz, D. Weygand, M. Zaiser and S. Zapperi, Science **318**, 251 (2007).
30. B. Devincre, T. Hoc and L.P. Kubin, Science **320**, 1745 (2008).
31. B. Devincre, private communication.
32. M. Babic, Int. J. Eng. Sci. 35, 523548 (1997).
33. A. Acharya, Proc. Roy. Soc., **A 459**, 1343 (2003).
34. M.J. Marcinkowsky, Phys. Stat. Sol. B **152**, 9 (1989).
35. C. Meneveau and J. O'Neil, Phys. Rev. E **49**, 2866 (1994).
36. P. Duval, M.F. Ashby and I. Anderman, J. Phys. Chem., **87**, 4066 (1983).
37. C. Shearwood and R.W. Whitworth, Phil. Mag., **64**, 289 (1991).
38. J. Chevy, Ph. D. Thesis, Institut Polytechnique de Grenoble (2008).
39. M. Montagnat, P. Duval, P. Bastie and B. Hamelin, Scripta Mater., **49**, 411 (2003).
40. M. Montagnat, J. Weiss, J. Chevy, P. Duval, H. Brunjail, P. Bastie and J. Gil Sevillano, Phil. Mag., **86**, 4259 (2006).
41. P.J. Armstrong and C.O. Frederick, *A mathematical representation of the multiaxial Bauschinger effect*, Technical Report RD/B/N/731, Central Electricity Generating Board (1966).
42. F. Louchet, C.R. Physique, **5**, 687 (2004).
43. H. Suzuki, S. Ikeda and S. Takeuchi, J. Phys. Soc. Japan, **11**, 382 (1956).
44. J. Weertman, Acta Mater., **50**, 673 (2002).
45. L.B. Zuev, Ann. Phys. **16**, 286-310 (2007).
46. A. Acharya, A.J. Beaudoin and R. Miller, Math. Mech. Solids **13**, 292 (2008).
47. S. Varadhan, A.J. Beaudoin and C. Fressengeas, Proc. of Science, SMPRI2005, 004 (2006).
48. O. Nittono, Jap. J. Appl. Phys., **10**, 188 (1971).
49. S.S. Brenner, J. Appl. Phys., **28**, 1023 (1957).
50. Y. Gotoh, Phys. Stat. Sol. (a), **24**, 305 (1974).
51. A. Piobert, Mémoires de l'artillerie, **5**, 502 (1842).
52. W. Lüders, Dinglers Polytech. J., **155**, 18 (1860).
53. A. H. Cottrell, *Dislocations and Plastic Flow in Crystals*, University Press, Oxford, (1953).
54. L.P. Kubin, Y. Estrin and C. Perrier, Acta Metall. Mater., **40**, 1037 (1992).
55. C.F. Tipper, J. Iron Steel Inst., **2**, 143 (1952).
56. D.V. Wilson and G.R. Ogram, J. Iron Steel Inst., 911-920 (1968).
57. R.A. Elliott, E. Orowan, T. Udoguchi, A.S. Argon, Mech. Mat., **36**, 1143 (2004).
58. L.P. Kubin and Y. Estrin, Acta Metall. Mater. **38**, 697 (1990).
59. A. Acharya and A.J. Beaudoin, J. Mech. Phys. Sol. **48**, 2213 (2000).
60. N. Louat, Scripta Metall. **15**, 1167 (1981).
61. P.G. McCormick, Acta Metall. **36**, 3061 (1988).
62. A. Ziegenbein, Ch. Achmus, J. Plessing and H. Neuhäuser, in *Plastic and Fracture Instabilities in Materials*, **200**, 101, ASME-AMD (1995).
63. T. Hasegawa, T. Yakou and S. Karashima, Mat. Sci. Engng., **20**, 267 (1975).

64. B. Peeters, S.R. Kalidindi, P. Van Houtte, E. Aernoudt, Acta Mater., **48**, 2123 (2000).
65. B. Peeters, S.R. Kalidindi, C. Teodosiu, P. Van Houtte, E. Aernoudt, J. Mech. Phys. Sol., **50**, 783 (2002).
66. S. Kok, M.S. Bharathi, A.J. Beaudoin, C. Fressengeas, G. Ananthakrishna, L.P. Kubin, M. Lebyodkin, Acta Mater., **51** 36513662 (2003).
67. J.W. Hutchinson and K. Neale, J. Mech. Phys. Sol. **31**, 405-426 (1983).
68. S. Varadhan, A.J. Beaudoin and C. Fressengeas, *Lattice incompatibility and strain-aging in single crystals*, submitted.